Applied Acoustics 242 (2026) 111045

Contents lists available at ScienceDirect

Applied Acoustics

journal homepage: www.elsevier.com/locate/apacoust

Experimental investigation on the application of serrated trailing edge propellers for drone noise reduction

Paolo Candeloro [a,*], Daniele Ragni [b], Tiziano Pagliaroli [a]

[a] Universitá degli Studi Niccoló Cusano, Engineering Department, Via Don Carlo Gnocchi 3, Roma, 00166, Italy
[b] Delft University of Technology, Flow Physics and Technology Department, Faculty of Aerospace Engineering, Kluyverweg 1, Delft, 2629HS, the Netherlands

ARTICLE INFO

Keywords:
Drones
Aerodynamics
Aeroacoustics
Rotor noise
Proper orthogonal decomposition

ABSTRACT

This study investigates a widely researched passive noise control strategy for reducing propeller trailing edge noise. The research aims to demonstrate how serrated drone blades can mitigate broadband noise components while simultaneously reducing tonal noise components. An experimental study involving the design, manufacture, and testing of 23 propellers was performed to establish a relationship between serration geometry and noise mitigation. Acoustic characterization during hovering was carried out at a constant rotational speed of $\Omega = 4000$ RPM using near-field microphone measurements. Subsequently, detailed aerodynamic and acoustic investigations were performed, employing load cells, Particle Image Velocimetry, and microphone array measurements in an anechoic wind tunnel. The tests were carried out at a constant rotational speed of $\Omega = 5000$ RPM and different advance ratios. The results indicate that by properly tuning the serration geometry, a significant reduction in both tonal and broadband noise components can be achieved, with reductions of 3 and 4 dB respectively. However, this comes with the drawback of a nearly 20% loss in thrust coefficient during advanced flight, as well as a 20% reduction in energy consumption. Broadband noise reduction is attributed to the cancellation of spanwise correlation length, while tonal noise is influenced by the reduced load on the blade and tip vortices intensity. Average and root mean square velocity fields reveal that serrated trailing edges promote the break up of peak vorticity in the tip-vortex region, potentially reducing interaction noise between the tip vortex and surrounding drone structures. Proper Orthogonal Decomposition (POD) analysis of the velocity field shows that serrations reduce trailing edge vorticity and tip vortices by shifting energy from large-scale to small-scale structures.

1. Introduction

The increasing diffusion of drones has driven renewed research interest in propeller-based propulsion systems [1], particularly for small-scale applications [2]. This interest is largely attributed to the advantages of these vehicles, including compact size, simple construction, excellent maneuverability, and vertical takeoff and landing capabilities [3]. With the drone market projected to reach €53.1 billion by 2025 [4], noise reduction has become a key factor in enhancing public acceptance and market competitiveness. Multicopters typically operate at low altitudes and in close proximity to populated areas, making propeller noise a critical concern. Despite their high rotational speeds, these propellers operate in a low Reynolds number regime, leading to unique aerodynamic and acoustic challenges. Noise optimization strategies have revealed the need for a trade-off between maximizing propeller thrust and reducing noise emissions, underscoring the importance of innovative approaches to propeller design and operational strategies [5–8].

Several studies on propeller noise can be found in literature, for example, see [8,5,6,9–16,7,17–19].

The use of trailing-edge (TE) serrations for noise reduction has been extensively studied in the literature. The theoretical basis was given by Howe [20,21], which stated that serrations mitigate noise through destructive interference of scattered surface pressure fluctuations. The noise mitigation is dependent on the serration height-to-wavelength ratio, with a reduction of $10\log_{10}\left[1+(4h/\lambda)^2\right]$, where h is the half-height and λ the wavelength of the serration. Moreover, Lyu et al. [22] and Huang [23] developed theoretical models demonstrating an achievable noise reduction of $10-20$ dB. In addition, different serration configurations have been addressed in the literature, including iron-shaped [24], combed-sawtooth [25,26], and slitted-sawtooth configurations [27,28]. Nevertheless, at the actual state of the art it is not available in the literature a design approach for TE serration.

* Corresponding author.
E-mail address: paolo.candeloro@unicusano.it (P. Candeloro).

https://doi.org/10.1016/j.apacoust.2025.111045
Received 28 June 2024; Received in revised form 27 August 2025; Accepted 27 August 2025

Available online 9 September 2025

Moreover, most studies have focused on add-on serrations, that may introduce unfavorable structural properties due to vibrations [29,30]. As an alternative, cut-in serrations, as in the present manuscript, have been explored [29,31,32] demonstrating comparable noise reduction effectiveness.

The application of serrations to rotors and wind turbines has given promising results. Aerodynamic and acoustic investigations on UAV rotors equipped with full-span serrated TE configurations have demonstrated systematic noise reduction between 0.9 and 1.6 dB while maintaining a constant thrust of 3 N [30,33]. Ning and Hu [30] also gives guidelines for the design of serration stating that $2b/h$, where b denotes the base and h the height of the tooth, must be lower than 4 to guarantee a noise effect. Additionally, serrations applied to hovering rotors have been found to suppress high-frequency broadband noise [17], however tonal noise levels at lower frequencies tend to increase at high rotational speeds.

Studies on varying serration depths indicate that beyond a certain depth threshold further noise reduction benefits are negligible [34]. Small-scale propellers with TE serration demonstrate a noise reduction up to 10 dB in the low frequency region. Such effect is associated with a damping in the tale of the distribution function [7,35]. Experimental tests on multicopter rotors equipped with cut-in serrations in both hovering and forward flight conditions have shown reductions of up to 8 dB in the high-frequency range [36]. Similarly, wind turbine blades with TE serrations achieved an average noise reduction of 3.2 dB [37].

One significant concern for the application of TE serrations is the impact on aerodynamic performance. For cut-in serrations, the lift coefficient and lift-to-drag ratio show slight increase in comparison to the BL model [29]. Lee et al. [38] experimentally investigated the noise and thrust variation of serrated propellers achieving a noise reduction of 5.8 dB at 3000 RPM. A preliminar explanation of noise reduction mechanism from flow field perspective was provided by Yang et al. [39,40]. Moreover, Gu et al. [3] demonstrated that the optimal design of a propeller with round serrations can achieve a noise reduction of approximately 64%, while limiting the increase in energy consumption to less than 5% at constant thrust.

The present manuscript aims to clarify whether serrated trailing edges can be used to reduce the noise produced by drone propellers. The objective of the present research activity is to establish a relation between the noise reduction and serration geometry. For this purpose, a comprehensive experimental investigation has been conducted, involving load cells, microphones, and Particle Image Velocimetry (PIV) measurements within an anechoic wind tunnel facility, to characterize the propulsion system and the control strategy proposed from aerodynamic and aeroacoustic point-of-view.

The manuscript is organized as follows: details on the design of the propellers, the experimental setup and the noise control strategy are addressed in Section 2. The main results are reported in Section 3 whereas conclusions and final remarks are given in Section 4.

2. Material and methods

2.1. Design of the serrated propellers

For the experimental campaign, a commercial propeller model APC $9 \times 4e$ was employed as baseline (BL) having a diameter of 228.6 mm and a pitch of 4 degrees. A total of 23 STE propellers were manufactured by removing material from the trailing edge.

The serration geometries considered had a base width b ranging from 3 to 6 mm and a height h between 3 and 8 mm, ensuring compliance with the constraint $2b/h < 4$. This condition guarantees a serration angle α below 45°, which is critical to achieve noise reduction [31,41,30].

Furthermore, the lower bound of b is dictated by the structural integrity of the material, while the upper bound of h is based on the findings of Intravartolo et al. [34], which demonstrate that exceeding 46% of the mean aerodynamic chord does not provide any additional noise reduction benefits. An additional parameter was considered: the number of teeth n. Therefore, for each analyzed geometry, two propellers were made: one with $n = 10$ teeth and another with $n = 5$.

The geometrical parameters are depicted in Fig. 1. The details of the test cases are provided in Table 1.

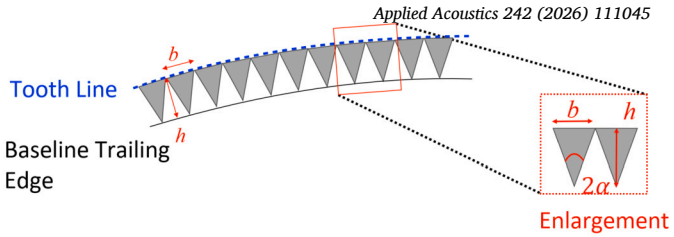

Fig. 1. Representation of the serrated trailing edge. In the enlargement the main geometrical parameters of the tooth are reported: tooth basis b, height h and the serration angle α.

Table 1
Test matrix of the preliminary measurement campaign where each case corresponds to a propeller.

Case	b_i [mm]	h_i [mm]	n	$2b/h$	Marker
1	4	4	10	2	
2	4	3	10	2.66	
3	4	6	10	1.33	
4	4	8	10	1	
5	4	4	5	2	
6	4	3	5	2.66	
7	4	6	5	1.33	
8	4	8	5	1	
9	5	3	10	3.33	
10	5	6	10	1.66	
11	5	4	5	2.5	
12	5	3	5	3.33	
13	5	6	5	1.66	
14	6	4	10	3	
15	6	6	10	2	
16	6	8	10	1.5	
17	6	6	5	2	
18	6	8	5	1.5	
19	3	3	10	2	
20	3	6	10	1	
21	3	8	10	0.75	
22	3	6	5	1	
23	3	8	5	0.75	

2.2. Experimental setup

The experimental analysis consisted of two activities: an acoustic study in hover conditions and an aeroacoustic characterization in both hover and advanced flight conditions.

2.2.1. Anechoic chamber experimental setup

The experimental tests were performed in the anechoic chamber of Niccolò Cusano University, which is 3x1.6x3 m in size. The propellers are driven by a brushless motor AXI 2204 and controlled by an Electronic Speed Controller Hobbywing Skywalker 20A. Measurements were performed at constant rotational speed $\Omega = 4000$ RPM, corresponding to a Reynolds number $Re_{0.75} = 2.5 \times 10^4$ and a tip Mach number $M = 0.12$. Pressure fluctuations were sampled by using Microphone Gefell M360 and National Instrument ACQ board type NI cDAQ-9174. The microphones present a free-field Sound Pressure Level that ranges from 30 to 135 dB, a diameter of 1/4 inch, and a frequency linear range between 20

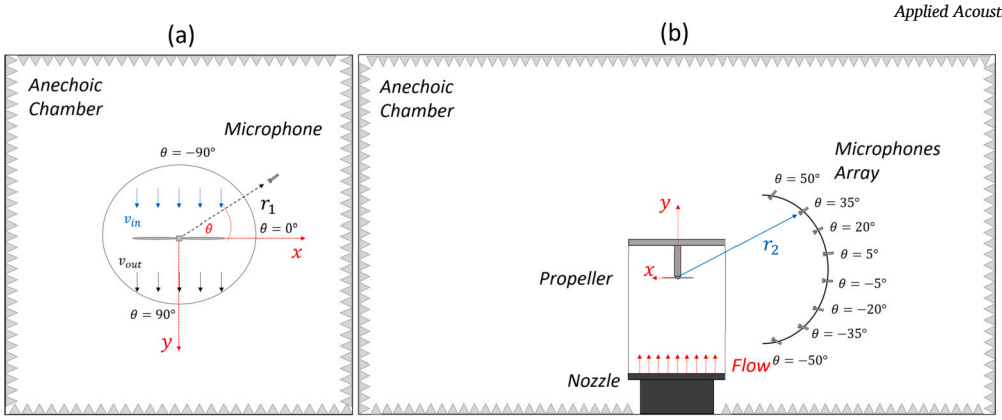

Fig. 2. Sketch of the experimental setup used for the acoustic qualification (a) and for the wind tunnel tests campaign(b).

Hz and 20 kHz. All pressure signals are acquired for 10 s at sampling frequency of 51.2 kHz. The microphone was mounted on a manual stage, allowing rotation within the polar angle θ from −90° to 60°, spanning from the suction side to the wake region of the propeller for conducting directivity analysis. The microphone was located within the near field, at a radial distance from the propeller disk $r = 460$ mm ≈ 2 D. The experimental setup and the polar reference system adopted are depicted in Fig. 2(a).

2.2.2. Wind tunnel experimental setup

The aerodynamic and aeroacoustic characterization was performed at the TUDelft University of Technology. The experimental tests were carried out in the A-Tunnel, a vertical, open-jet wind tunnel, where the surrounding of the nozzle outlet consists of an anechoic chamber as depicted in Fig. 2(b). The exit nozzle is circular with a diameter of 0.60 m. The low cut-off frequency of the anechoic chamber is about 200 Hz. The measurements were conducted in 3 operative condition $\Omega = 4000$ RPM, $\Omega = 5000$ RPM and $\Omega = 6000$ RPM. Moreover, the inflow velocity was varied in the range from 0, to simulate hover condition, to 11 m/s corresponding to an advance ratio $J = \frac{v}{nD}$ ranging from 0 to 0.6 (the zero-thrust condition for the baseline propeller).

The propeller is connected to a profiled aluminum nacelle for minimum interference with the propeller flow, the instrumentation (composed of a motor, an encoder, a load cell, and a torque cell) is embedded in the nacelle. The nacelle is supported by stiffened hollow aluminum NACA0012 profiles of 60 mm chord. Nacelle and vertical support are used as cable routing of the power supply, cables for encoder and load cells, and even motor control signals. The entire structure is held up above the nozzle of the tunnel by 4 steel-wire tubes of 20 mm diameter fixed to the tunnel to avoid vibrations. The propeller is driven by an electric brushless motor Leopard Hobby 3536-5T 1520 KV with a diameter of 27.8 mm and a maximum power of 550 W. The motor is powered by a Delta Elektronika DC power supply with a voltage range of 0 - 15 V and a current range of 0 - 100 A. The motor rotational speed is measured by means of a US Digital EM1 transmissive optical encoder, coupled with a US Digital disk of 1 in diameter and 200 pulses per revolution. Rotor thrust is measured using a Futek LSB200 load cell excited with 5 VDC. The load cell is characterized by a maximum capacity of 22.2 N, nonlinearity and hysteresis of ± 0.1% of RO, and an operating temperature between -50 to 90 °C. The torque is measured using a Transducer Techniques RTS-25 torque sensor excited with 10 VDC. It has a maximum capacity of 0.18 Nm, nonlinearity and hysteresis of ± 0.1% of RO and an operating temperature between -54 to 93 °C. The thrust and torque signals are acquired by a National Instrument acquisition board with a sampling frequency of 5 kHz and an acquisition time of 30 s.

Far-field noise measurements are performed employing microphones mounted on a semicircular array, centered at the propeller axis, as sketched in Fig. 2(b). The array has a radius of $r = 1.20$ m $= 5D$ and is constituted by 4 LinearX M51 and 4 LinerarX M53 free field microphones, with a maximum SPL of 150 dB and 130 dB respectively, a diameter of 1/2 inch and a frequency linear range between 20 Hz and 20 kHz. The Data Acquisition System (DAS) consisted of two National Instrument modules NI9234. A polar reference system has been adopted to define the angular position of each microphone with respect to the propeller center, the reference system is defined in Fig. 2(b). Pressure fluctuation time histories have been recorded for 30 s at a sampling rate of $f_s = 51200$ Hz.

Thereafter, a stereoscopic PIV investigation was conducted to measure the propeller flow field. Sets of 500 images have been recorded. The flow is seeded with particles of 1-micron median diameter produced by a SAFEX Twin Fog generator with SAFEX-Inside-Nebelfluid, a mixture of dyethelene glycol and water. The particles are introduced in the wind tunnel circuit to ensure a uniform concentration while recirculating. Illumination of the field of view is provided by a double cavity Quantel EVerGreen EVG00200 Nd:YAG laser with 200 mJ/pulse energy. A schematic representation of the stereoscopic PIV setup is shown in Fig. 3, which also reports the generation of the laser beam and its conversion into a laser sheet of 2 mm through light optics. The laser sheet is aligned with the propeller axis of rotation. Two Imager sCMOS cameras with 2560 × 2160 pixels and four Nikon lenses with 50 mm focal length at f# 8 have been used for the measurements. In order to align the measurement plane with the focal plane, Scheimpflug adapters have been mounted on each camera. The camera calibration, acquisition, and post-processing have been carried out with the LaVision Davis 8.4 software. The images are processed with a window deformation iterative multi-grid with a final interrogation window size of 16 × 16 pixels and 50% overlap. Spurious vectors are isolated through a median filter and replaced by interpolation. Details of the PIV setup apparatus are given in Tables 2 and 3.

Table 2
Details of Imaging Parameters.

Imaging Parameters	
Camera	2 Imager sCMOS
Number of pixels [px]	2560 x 2160
Pixel size [μm]	6.5 x 6.5
Focal length [mm]	50
Magnification	0.05
FOV [cm^2]	35 x 35
Imaging resolution [px/mm]	8

3. Results and discussions

3.1. Noise assessment in the near field during hover

The initial phase of the investigation aims to investigate the serrations influence on noise emissions. For this purpose, the OverAll Sound

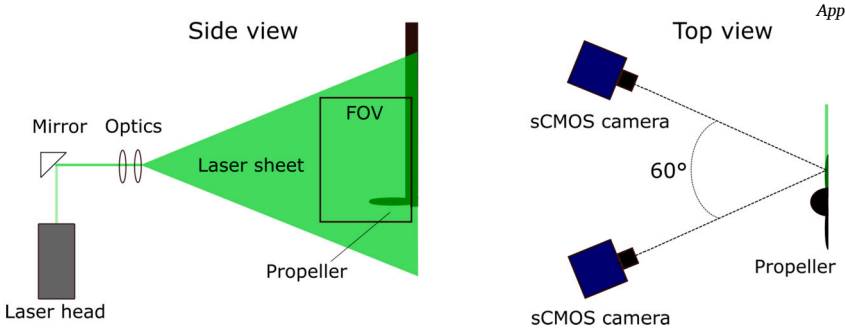

Fig. 3. Schematic representation of the stereoscopic PIV setup: (left) side view, (right) top view.

Table 3
Details of PIV Parameters.

PIV Parameters	
Software	LaVision Davis 8.4
Pulse separation [μs]	10
Number of recordings	500
Windows size [px^2]	16 x 16

Table 4
Test cases under investigation.

Test Case	b [mm]	h [mm]	AR_t [−]	Number of teeth	$\Delta S\%$
STE 1	4	3	2.66	5	2
STE 2	6	6	2	10	10

Pressure Level (*OASPL*) of each propeller was calculated in different angular positions. For brevity, only the results regarding the rotor plane, identified by $\theta = 0°$, and the wake region, identified by $\theta = 30°$ and $\theta = 60°$, are reported as they are considered of primary interest, as they simulate the condition of a drone flying above people, the obtained results are plotted in Fig. 4. For the definition of the polar angle see Fig. 2(a).
The OASPL was computed as:

$$OASPL = 10\log_{10}\left(\frac{\sigma_P}{p_{ref}}\right)^2 \tag{1}$$

where the σ_P is the standard deviation of the pressure time series evaluated as:

$$\sigma_P^2 = \int_{f_1}^{f_2} PSD(f)\,df \tag{2}$$

where f_1 and f_2, the extremes of the region of interest, are set to cover the entire microphone linear operating range, and the PSD is the Power Spectral Density of the pressure signal expressed in Pa^2/Hz. Moreover, p_{ref} is the reference pressure equal to 20 μPa (threshold of human hearing).
In Fig. 4, a red dash-dotted line representing the OASPL associated with the BL propeller (i.e., a propeller without trailing edge serrations) was included in each plot to provide a reference point. The most prominent result is that the noise source exhibits strong directivity. Such characteristic complicates the acoustic optimization of propellers. On the contrary, efforts must be focused on targeting specific regions for noise reduction. Regarding the results in the rotor plane (Fig. 4(a)), it can be observed that all test cases, except one, demonstrate a reduction in the OASPL. Moving towards the wake region, it is observed that at $\theta = 30°$ (Fig. 4(b)), some STE propellers produce higher noise levels compared to the baseline, while at $\theta = 60°$ (Fig. 4(c)), a significant mitigation in acoustic emissions is observed, involving all investigated STE propellers except for a single case. This behavior underscores the variability in acoustic emissions across different configurations, each defined by unique combinations of the geometric parameters under consideration. As a result, the criterion $2b/h < 4$ does not ensure noise reduction. These findings challenge the validity of existing models and raise questions about the necessity of developing dedicated models to address this specific scenario. These considerations validate the present work as it can serve as a starting point for the development of a mathematical framework to study propeller serrations. Moreover, as one transitions from the rotor plane (Fig. 4(a)) to the wake region (Fig. 4(c)), the serrations influence becomes increasingly pronounced.
One of the objectives of this analysis was to identify, among all the considered test cases, those of greatest interest in order to focus the rest of the study on them. It was decided to focus on the wake region as it is considered of primary interest. The test cases with the highest and lowest acoustic impact, as indicated by red circles in Fig. 4(c), were selected for further investigation and labeled as STE1 and STE2 in the following. The geometrical parameters of these cases are detailed in Table 4.
One of the objectives of this study is to support the design of serrations. For this purpose, Fig. 5 presents the variation of the OASPL at $\theta = 60°$ by first fixing the height h (Fig. 5(a))) and then the base b (Fig. 5(b)), with a constant serration number $n = 10$ in both cases. The results for varying h align with the findings of Intravartolo et al. [34], which indicate that once the ratio h/c exceeds 46.67%, the acoustic benefits of serrations become less effective. Indeed, Fig. 5(a) shows that increasing h initially improves the acoustic performance, but a degradation is observed at $h/c = 0.58$. Notably, in this range, the presence of serrations consistently provides an acoustic benefit compared to the BL. On the other hand, regarding the effect of b, the results show that increasing this parameter enhances the acoustic performance, in agreement with Moreau and Doolan [42], Moreau et al. [43]. Consequently, in the design of the sawtooth pattern, it is preferable to employ wider teeth while maintaining a serration depth below 40%. From the results in Fig. 4(c), the optimal value of $2b/h$ for the best acoustic performance is found to be 2.
To further characterize the acoustic source, the variation of OASPL concerning the polar angle θ is reported for only these two configurations. The results are reported in the Fig. 6(a). In this case, as well, the results related to the baseline propeller are included for comparison. From these observations, it can be noted that the presence of serrations does not ensure a consistent acoustic effect; rather, preferred directions exist where changes in the acoustic impact occur. Specifically, STE2 exhibits a noticeable decrease in noise for θ values greater than 0°, whereas, for negative polar angles, the reduction is less pronounced. Moreover, for STE1 a slight increase in the noise produced is observed for positive polar angles, which becomes more evident for negative polar angles. To quantify which noise component the measured effects were associated with, the Band-Limited Sound Pressure Level (*BLSPL*) was computed at various polar angles. Specifically, it can be calculated as in [44,45]:

$$BLSPL = 20\log_{10}\left(\frac{\sigma_P}{p_{ref}}\right) \tag{3}$$

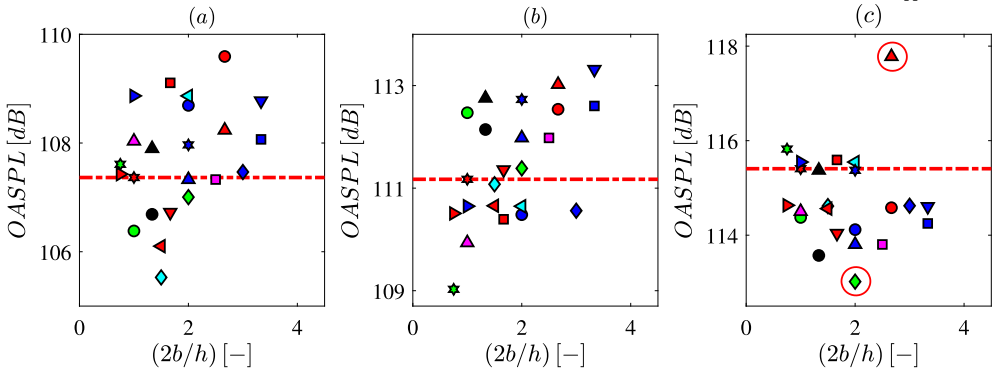

Fig. 4. OASPL measured for all the test cases as a function of the tooth aspect ratio $2b/h$ at constant rotational velocity $\Omega = 4000$ RPM for three polar angle stages: $\theta = 0°$ (a); $\theta = 30°$ (b); $\theta = 60°$ (c). The red dash-dotted line represents the baseline propeller as a reference.

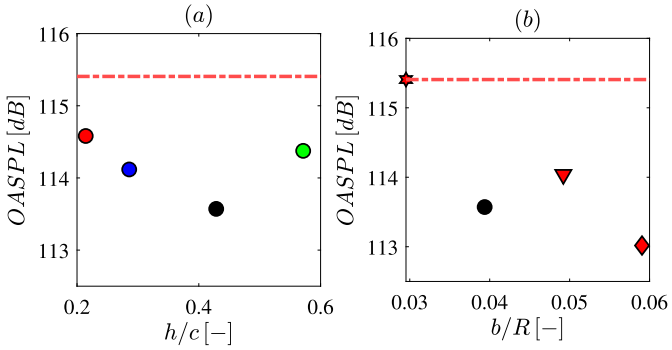

Fig. 5. OASPL measured at constant value of the tooth basis $b = 4$ mm (a) and constant tooth height $h = 6$ mm (b) for polar angle $\theta = 60°$. The red dash-dotted line represents the baseline propeller as a reference.

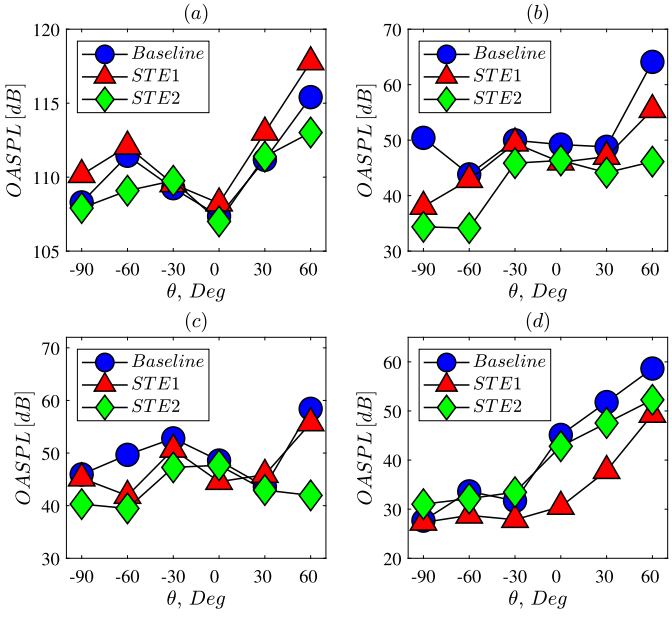

Fig. 6. Polar plot of the OASPL for the baseline, the STE1 and STE2 propellers at constant rotation speed $\Omega = 4000$ RPM: Overall SPL (a), Band-Limited SPL in the Low-frequency region (b), the First harmonic (c), and the Second harmonic (d).

using the definition of σ_P given in Eq. (2) with the appropriate frequencies range. Specifically, the analysis focused on the low-frequency region (Fig. 6(b)) and the first (Fig. 6(c)) and the second (Fig. 6(d)) harmonics. The selected regions have been selected for several reasons. The tonal component, primarily responsible for annoyance, is linked to blade loading. Implemented as described in this study, serrations have effectively reduced the blade surface area. A decrease in thrust and in the tonal noise produced is expected. Regarding the broadband component, it is known from Amiet's theory that serrations will modify the power spectral density [46,47]. Previous studies have shown that this effect is more pronounced at lower frequencies [7]. Hence, our focus was on a frequency range from the microphone's lower acquisition limit up to the first harmonic. The main result is that the STE2 propeller demonstrates a reduction across the entire polar plot, both in the low-frequency region (Fig. 6(b)) and for the first harmonic (Fig. 6(c)), while the STE1 shows a minor modification for the first harmonic that becomes more significant at the second harmonic (Fig. 6(d)). These findings, along with those from the ensemble, suggest that by varying the tooth geometry, it may be possible to affect different frequencies. Such an effect opens up various application possibilities.

Furthermore, focusing on $\theta = 60°$ case a spectral and a statistical analysis is provided and the results were compared to those of the baseline propeller. The spectra are presented in the normalized form of the Sound Pressure Spectrum Level (*SPSL*), that according to [48–50], is calculated as:

$$SPSL = 10\log_{10}\left(\frac{PSD\,\Delta f}{p_{ref}^2}\right) \tag{4}$$

where Δf is the frequency resolution equal to 1 Hz. Moreover, the noise spectra are represented as a function of the Harmonics of the Blade Passing Frequency defined as:

$$HBPF = \frac{2\pi f}{B\Omega} \tag{5}$$

where f is the frequency, B is the blade number and Ω is the propeller rotational velocity.

The obtained results are consistent with the previous findings, providing further insights. Specifically, a dual phenomenon is observed. More in detail, in Fig. 7(a), for $HBPF = 1$, a significant reduction effect on the tonal component is observed for STE2, quantifiable at 12 dB. Additionally, both STE1 and STE2 show a reduction of approximately 10 dB compared to the baseline for the second harmonic. The effect on the broadband component is even more evident for $HBPF < 1$, where both STE propellers show a reduction in terms of SPSL. This effect is observed for all frequencies for the STE2 propeller, while STE1, beyond the first harmonic, tends to behave similarly to the baseline. This observed effect on the tonal component could suggest a reduction in the thrust generated by the propeller, as will be analyzed later, but it remains highly

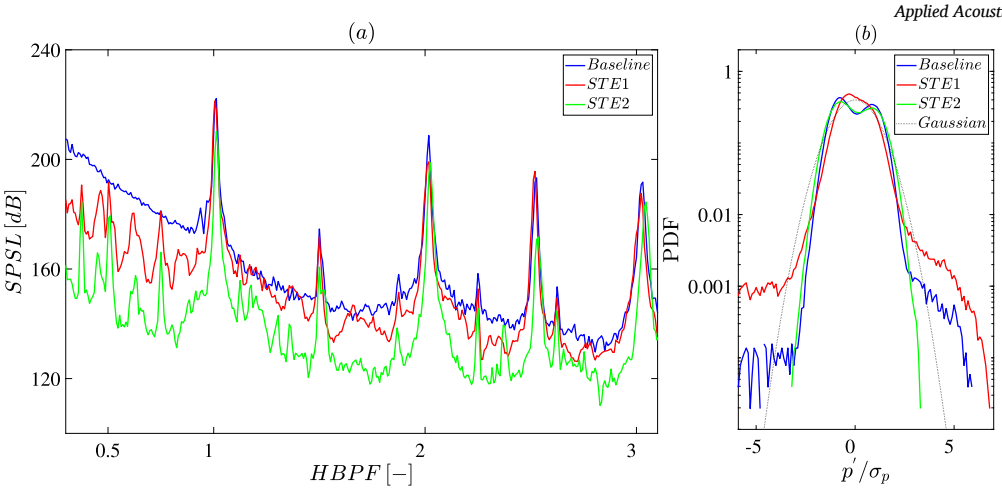

Fig. 7. Dimensionless spectra(a) and Probability Density Function of the near-field pressure signals for the STE1 and the STE2 blade at constant rotational velocity $\Omega = 4000\,RPM$ in comparison with the baseline propeller for the polar angle $\theta = 60°$.

intriguing. Since, by employing serrations, it is thus feasible to manage both noise components. These findings are further supported by the examination of the Probability Density Function (PDF) of the pressure time histories reported in Fig. 7(b). The variable is represented in a reduced form to achieve a zero mean and unit standard deviation. The PDFs exhibit a bimodal behavior, more pronounced for the baseline propeller and STE2, characteristic of a periodic phenomenon as the present one. However, a deviation from the Gaussian distribution is observed for the baseline propeller. This effect is exacerbated by the STE1 propeller and canceled by the STE2. Such deviations in the distribution tails are commonly associated with intermittent phenomena embedded in the pressure time series, known to contribute to broadband noise.

This allows us to provide an initial interpretation of the serration effect. By properly modifying the trailing edge, the spanwise correlation length is reduced, leading to a decrease in broadband noise as coherent structures embedded in the time history are eliminated. Conversely, if geometric parameters are incorrect, the intermittency phenomenon is exacerbated, resulting in an overall increase in noise production.

3.2. Characterization of aerodynamic and aeroacoustic aspects

An aerodynamic characterization was performed in terms of thrust and power coefficient c_T and c_P. The results are reported in Fig. 8 for both hovering and advanced flight conditions. For the sake of brevity only the results regarding the rotational speed $\Omega = 5000\,RPM$, corresponding to a Reynolds number $Re_{0.75} = 3.08 \times 10^4$ and a tip Mach number $M = 0.15$, are reported in the present study. The inflow velocity is expressed in dimensionless form as the Advance Ratio $J = \frac{v_\infty}{nD}$, where v_∞ represents the inflow velocity, n is the rotational velocity in Hz, and D is the propeller diameter. The range of Advance Ratio considered spans from $J = 0$ to $J = 0.6$, with the upper limit set at the condition of zero thrust. The thrust coefficient is defined as in [51]:

$$c_T = \frac{T}{\frac{1}{2}\rho\hat{S}V^2} = \frac{T}{\frac{1}{2}\rho\hat{S}(\Omega\frac{D}{2})^2} \tag{6}$$

where T is the thrust force expressed in N, ρ the air density kept constant at 1.225 kg/m^3, $\hat{S}$ is the effective surface of the propeller, Ω the rotational frequency expressed in rad/s and D the propeller diameter in m. The employed formulation differs from the typical one commonly used for rotors, as discussed in various studies [52]. This choice was made to account for the variations in the lifting surface among the propellers so that the observed differences in the thrust coefficient (c_T) can be attributed to flow modifications. Similarly, the power coefficient is expressed as:

$$c_P = \frac{P}{\frac{1}{2}\rho\hat{S}V^3} = \frac{Q\Omega}{\frac{1}{2}\rho\hat{S}\Omega^3\frac{D}{2}^3} = \frac{Q}{\frac{1}{2}\rho\hat{S}\Omega^2\frac{D}{2}^3} \tag{7}$$

Fig. 8 reveals a significant decrease in the c_T, particularly for the STE2 propeller. Similar results are reported in the literature [30,39]. It has been demonstrated that a longer tooth length induces a greater loss of thrust [34,7]. Furthermore, the c_T reduction involves both the hovering (Fig. 8(a)) and the advanced flight conditions (Fig. 8(b)). Specifically, in hovering, the decrease in c_T is less than 5% for the STE1 propeller, while it reaches 12% for the STE2 propeller. In advanced flight, the impact on thrust generation is more significant, with a reduction of 10% and 20% for the STE1 and STE2 propellers, respectively. Such effects highlight the importance of proper serration design for a successful mission.

Furthermore, serrations not only affect the thrust coefficient but also the power coefficient, as observed in Fig. 8(c)-(d). A noticeable reduction compared to the BL can be observed for this coefficient in the presence of serrations, with the STE1 propeller exhibiting a reduction of approximately 2% in hovering, increasing to 3-4% during forward flight. For the STE2 propeller a reduction of approximately 14% in hovering and 20% during forward flight is observed. The reduction in energy consumption has been previously discussed in the literature [39], while the increase in consumption due to the presence of serrations reaches a maximum of approximately 10%. This result is consistent with the trends reported in Fig. 8 and does not introduce significant operational constraints for the drone, leading to a slight reduction in endurance. This effect is associated with the downstream displacement of wake vortices due to serrations, resulting in increased trailing-edge pressure and reduced pressure drag. A similar mechanism is utilized for flow control on blunt trailing-edge airfoils [53]. These features of TE serration make them favorable to UAV manufacturers from an aerodynamic point-of-view.

Having previously assessed the serration effect in the near-field, in the present paragraph the results concerning the far-field microphone measurements are presented. To maintain brevity, the manuscript focuses exclusively on the results related to the advanced flight conditions at a constant advance ratio $J = 0.36$. This value has been chosen as it is representative of a typical operating condition for a small-size drone. Initially, the OASPL has been calculated and the results are reported in Fig. 9 in the form of directivity diagram. The polar angle is defined as illustrated in Fig. 2(b). The main outcome is a relevant noise level reduction for both propellers. The mitigation ranges between 3

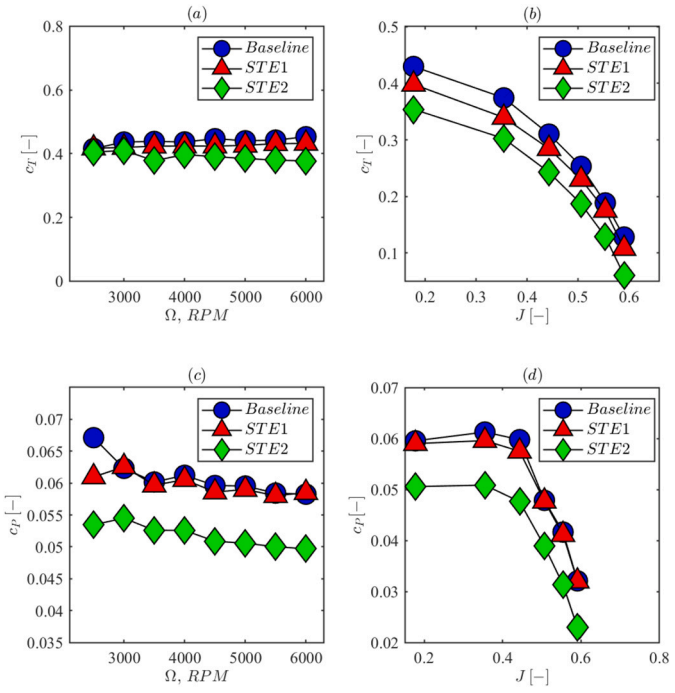

Fig. 8. Thrust coefficient c_T and Power coefficient c_P trend in hovering (a)-(c) and in advanced flight (b)-(d) conditions.

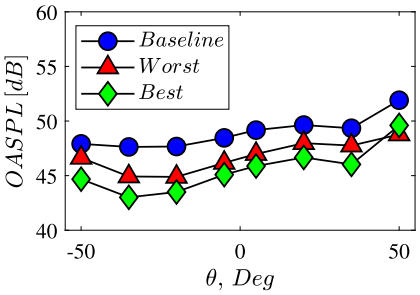

Fig. 9. OASPL measured at different polar angle θ and advanced flight condition; the inflow velocity is $V_\infty = 6$ m/s ($J = 0.36$) and the rotational velocity is $\Omega = 5000$ RPM. The ∘ represents the baseline propeller, the △ the STE1 propeller and the ⋄ line the STE2 propeller.

and 4 dB for the STE2 propeller, whereas the STE1 propeller induces an approximate reduction of 2 dB. In addition, such an effect is independent of the polar angle θ, the forward flight case exhibits a more substantial decrease in the thrust coefficient compared to the hover case. However, this reduction is coupled with a more favorable acoustic gain.

A spectral analysis of the wake region at $\theta = 50°$ in forward flight is conducted to compare with hover conditions, showing consistent results (Fig. 10). A reduction in noise can be observed in the low-frequency region for both STE propellers compared to the baseline, in particular the STE propellers cancel the two peaks for the baseline propeller in the region $HBPF < 1$. The effect is quantificable in 10 dB. In addition, a slight decrease in the tonal component is observed for the STE propellers of almost 3 dB. As expected, in the case of forward flight, the effects of the serrations are still present, although less intense. Furthermore, a reduction of 4-5 dB in the broadband noise component is observed in the region beyond the third blade passing frequency (BPF), consistent with previous findings by Wang et al. [54], Treuren and Wisniewski [55]. This effect is attributed to the attenuation of blade-wake interactions induced by the serrations. Furthermore, the reduction in broadband noise can be associated to the serrated structure, which disrupts large-scale vortices [3], leading to a decrease in l_y and consequently mitigating this noise component [8]. This effect on the broadband component can be explained by the analysis of the probability density functions (PDFs) in the Fig. 10. As in Fig. 7(b), a reduction in the tails of the distribution can be observed, this time involving both STE propellers. As a result, with the wind tunnel switched on, the STE propellers exhibit similar acoustic behavior, confirmed by both the spectral and the statistical analysis. In forward flight, the STE2 propeller, which performed better in hover, experiences a greater loss in thrust coefficient compared to STE1, while the acoustic benefit is less pronounced. This is because part of the blade is stalled, reducing the effective number of teeth influencing the acoustic performance. This phenomenon is crucial for serration design, suggesting that modifying the entire trailing edge geometry is unnecessary. Instead, adjustments should focus solely on the region near the tip, which serves as the primary working area.

3.2.1. *Time-frequency analysis in wavelet domain*

The acoustic behavior is also investigated through a time-frequency analysis in wavelet domain. Continous Wavelet Transform (CWT) is a powerful tool to achieve a detailed investigation into the temporal localization of acoustic characteristics across various frequencies. Unlike Fourier transform methods, which only offer frequency information, CWT provides a comprehensive understanding of how these acoustic properties evolve over time, crucial for identifying transient or intermittent phenomena in propeller acoustics [56,57]. Additionally, WT is highly effective in capturing and characterizing various types of non-sinusoidal periodic patterns, providing a deeper understanding of their underlying dynamics. In this regard, WT offers advantages over the classical Fourier representation [58]. For a more detailed overview, the authors recommend the comprehensive reviews available in Camussi and Guj [59], Farge [56], Mallat [60], Daubechies [61], Torrence and Compo [62]. CWT has been intensively applied to aeroacoustics in recent years due to its specific properties [63–65,15].

The process to perform a CWT involves the convolution between the time-dependent signal $x(t)$ and the *Mother Wavelet* $\Psi(t)$, in the present study, the chosen mother wavelet is the Morlet function, that is a plane wave modulated by gaussian envelope of unit width. As a result, the continuous WT is defined as:

$$w(s,\tau) = s^{-1/2} \int_{-\infty}^{\infty} x(t)\psi^* \left(\frac{t-\tau}{s}\right) dt \tag{8}$$

where $w(s,\tau)$ are the wavelet coefficient, ψ^* is the complex conjugate of the dilated and translated mother wavelet function, s is the scaling parameter and τ is the time shifting.

The results in terms of wavelet scalogram are presented in Fig. 11 for the forward flight case at $J = 0.36$ and rotational speed $\Omega = 5200$ RPM for the baseline propeller (a), STE1 (b), and STE2 (c). Due to its definition, the use of the WT allows for a detailed characterization of the tonal component. The main result observable in Fig. 11 is that all three propellers exhibit a fluctuating tonal component. Instead of a continuous streak for $HBPF = 1$, a patchy behavior is evident. Notably, these patches tend to disappear for the STE2 propeller, whereas the baseline and STE1 propellers exhibit very similar intensity levels. This further supports the tonal reduction observed in Fig. 10(a) while also providing additional insight. It can be stated that the reduction in the tonal component is not only related to a decrease in blade loading but also to the elimination of fluctuations within the same component. Furthermore, as seen in Fig. 10(a), a fluctuating component is present at $HBPF = 0.5$, that can be associated with the characteristic frequency of the motor. For the STE2 propeller, this component is entirely canceled, whereas it persists for STE1 due to reduced power absorption. As shown in Fig. 8(d), serrations decrease aerodynamic drag, lowering power consumption at a fixed rotational speed and reducing the motor's tonal component.

These results provide valuable insights for optimizing the design of serrations. As demonstrated by Moreau et al. [43], Moreau and

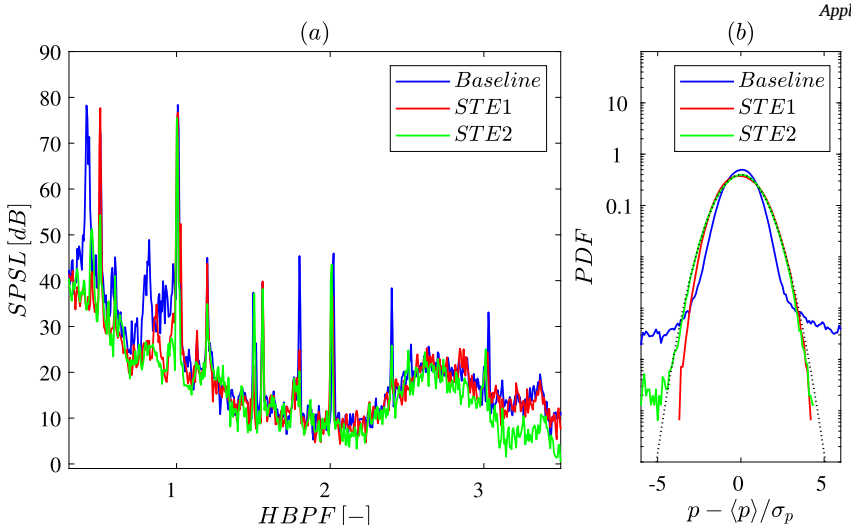

Fig. 10. Dimensionless spectra(a) and Probability Density Function of the far-field pressure signals for the STE1 and the STE2 blade at constant rotational velocity $\Omega = 5000$ RPM and inflow velocity $V_\infty = 6$ m/s ($J = 0.36$) in comparison with the baseline propeller for the polar angle $\theta = 50°$.

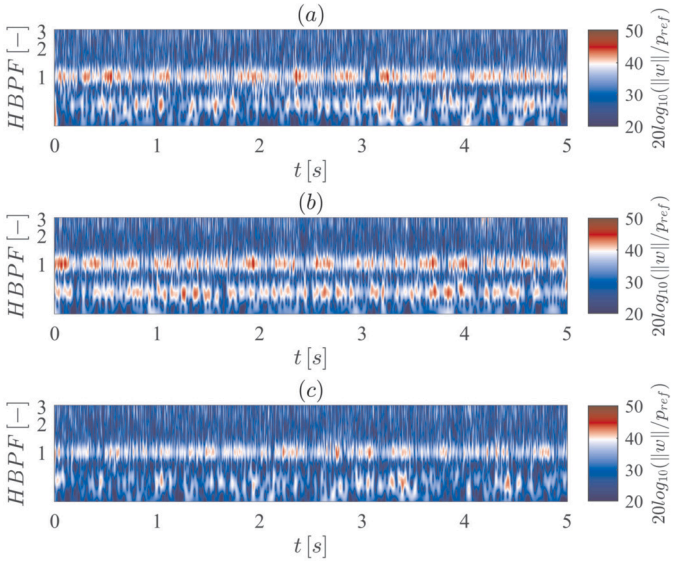

Fig. 11. Time-frequency representation of the wavelet intensity of the pressure fluctuations sampled by microphones positioned at $\theta = 50°$ at constant rotational velocity $\Omega = 5000\,RPM$ and inflow velocity $V_\infty = 6$ m/s ($J = 0.36$) for the baseline (a), the STE1 (b) and STE2 (c) propellers.

Doolan [42], wider serrations are more effective in noise reduction. Furthermore, it is observed that longer serrations contribute to greater noise attenuation. However, [34] showed that once the serration length exceeds 46% of the mean aerodynamic chord, no additional noise reduction benefits are achieved. Considering the constraint reported by [30,33], the present results indicate that an aspect ratio of $2b/h = 2$ is acoustically advantageous.

3.3. Analysis of the velocity fields

In order to understand how serrations impact the flow around the blade and establish a correlation with noise generation, a stereoscopic Particle Image Velocimetry (PIV) analysis of the propeller slipstream was conducted. For the sake of brevity only the results concerning constant rotational speed of $\Omega = 5000$ RPM and advance ratio $J = 0.36$ are included.

The average velocity and root main square velocity distributions within the propeller slipstream are reported in Fig. 12 in the first and second rows, respectively. The reference system is centered at the propeller hub, as depicted in Fig. 2(b), the x and y axis are normalized relative to the propeller diameter. The flow is aligned with the y-axis. The average velocity fields reveal an increase in the axial velocity downstream for all the propellers. More in detail, the wake velocity for the baseline and STE1 propellers (Figs. 12(a)-(b)) exhibits similar values. Whereas, the STE2 propeller demonstrates a reduction in wake velocity. This aspect is more evident in Fig. 13, which reports the velocity profiles for the three propellers at three different stations across the slipstream, respectively, $y/D = 0.2$ (a), $y/D = 0.4$ (b) and $y/D = 0.6$ (c). As observed previously, the STE1 and baseline propellers exhibit nearly identical maximum velocity, while the best propeller demonstrates a reduction of approximately 20% compared to the baseline. Furthermore, the serrations also affect the distribution of induced velocity along the x-direction. The x-position of the maximum velocity for the STE2 propeller differs from that of the STE1 propeller and is closer to the propeller root. Moreover, the rms velocity contour in the second row of Fig. 12 emphasizes that the majority of velocity fluctuations are related to the generation of tip vortices, which are subsequently shed into the wake. The intensity of the tip vortex generated by the STE1 propeller (Fig. 12(e)) is slightly lower compared to the baseline. Additionally, it is evident that the tip vortex for the STE2 propeller is almost canceled (Fig. 12(f)). These results confirm that the serration leads to a faster dissipation and a reduced trailing edge vorticity sheet intensity. Tip vortices are, in agreement with Pang et al. [17], Kim et al. [66], Miljković et al. [67], associated with unsteady noise generated by blade-vortex interaction as well as tonal noise. Therefore, the observed reduction involving both noise component can be attributed to this phenomenon.

To investigate the shedding of vorticity along the blade trailing edge and its impact on wake dynamics, Phase-locked (PL)-PIV measurements were performed. In Fig. 14, the rms velocity distribution is presented for three distinct phases. In this figure the baseline propeller is addressed in the first row, the STE1 propeller in the second row, and the STE2 propeller in the third row. The PL-PIV analysis reveals the generation of the trailing edge vorticity sheet at the rotor plane, depicted in Figs. 14 (a)-(d)-(g). Subsequently, this vorticity sheet is released into the wake, as illustrated in Figs. 14 (b)-(e)-(h), and further travels downstream, as seen in Figs. 14(c)-(f)-(i). The performance of the STE2 propeller is particularly noteworthy, as the rms velocity distribution displays clear evidence of the serration pattern. This observation indicates a disruption in the spanwise correlation length which cause a mitigation of TE noise [8]. It can be concluded that the implementation of serrations at the trailing edge reduces and, in specific configurations, eliminates a

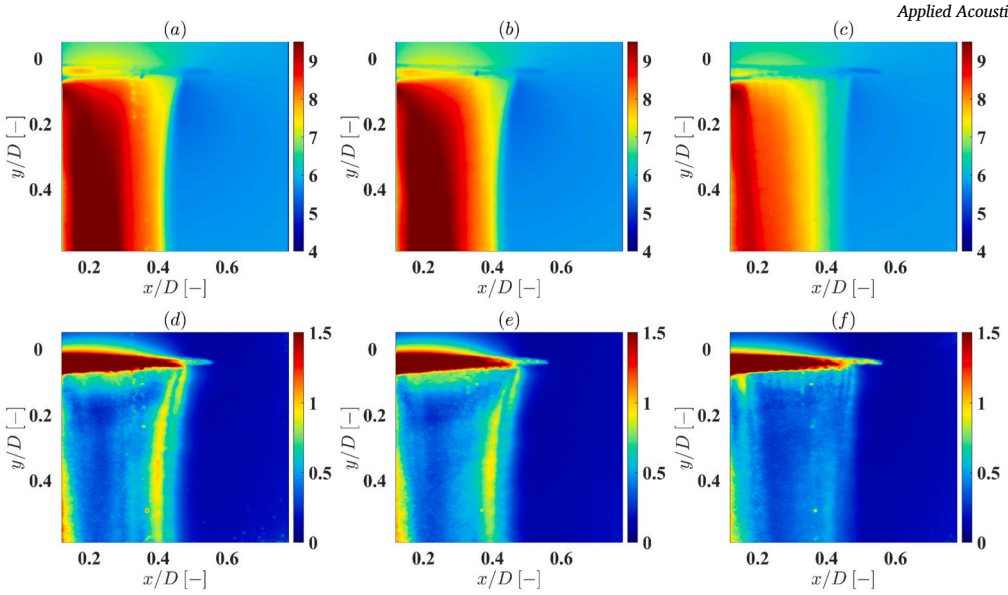

Fig. 12. Average velocity field for the baseline propeller(a), the STE1 propeller (b) and the STE2 propeller (c). RMS velocity field for the baseline propeller (d), the ST1 propeller (e), and the STE2 propeller (f). Contour plot obtained at constant inflow velocity $v_\infty = 6\,\mathrm{m/s}$ and rotational speed $\Omega = 5000\,RPM$.

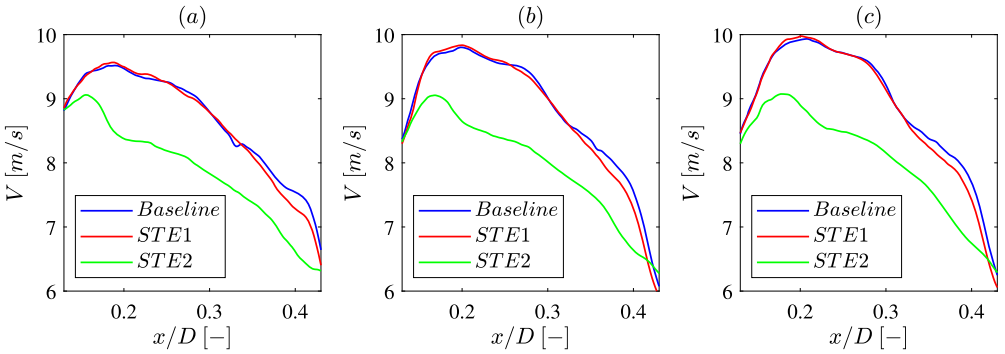

Fig. 13. Average velocity profiles at (a) $y/D = 0.2$, (b) $y/D = 0.4$ and (c) $y/D = 0.6$ for inflow velocity $v_\infty = 6\,\mathrm{m/s}$ and rotational speed $\Omega = 5000\,RPM$.

key source of tonal noise. This observation explains the dual effect observed in the Fourier domain and indicates that the reduction in tonal noise is not solely due to the loss of thrust.

3.3.1. *Proper orthogonal decomposition of the velocities fluctuations*

A Proper Orthogonal Decomposition (*POD*) analysis was conducted to identify the most energetic structures in the flow field and the impact of serrations on them.

Proper Orthogonal Decomposition (POD) is a mathematical technique initially introduced by [68] in hydrodynamics to extract a basis for modal decomposition from an ensemble of signals. For a detailed analytical formulation the authors suggest [69–71,63,15,72–75]. POD provides a mathematical model to decouple, from a turbulent field, spatial and temporal variations, judged essential according to energetic criteria. As a result, the flow is decomposed into both time and space orthogonal modes which are inherently related, in the sense that each space component is associated with a time component partner and vice versa. In particular, the performed analysis is the so-called “Snapshot POD”, presented by Sirovich [71]. Thereby, with the term *snapshot* each instantaneous PIV measurement is indicated, since, in the present study, the analysis is performed on 500 snapshots for each test case. A preliminary step is to calculate the mean velocity field that can be intended as the POD mode of order zero. The further study concerns the fluctuating part $\mathbf{V} = (u, v, w)^T$ (where u is the x-component, v is the y-component and w the z-component) of the velocity field.

The fluctuating component is organized in a matrix, called the Snapshot Matrix:

$$\mathbf{U} = \left[\mathbf{u}_1^1 \mathbf{u}_1^2 \cdots \mathbf{u}_1^N\right] = \begin{bmatrix} u_1^1 & u_1^2 & \cdots & u_1^N \\ u_2^1 & u_2^2 & \cdots & u_2^N \\ \vdots & \cdots & \cdots & \vdots \\ u_M^1 & u_M^2 & \cdots & u_M^N \\ v_1^1 & v_1^2 & \cdots & v_1^N \\ v_2^1 & v_2^2 & \cdots & v_2^N \\ \vdots & \cdots & \cdots & \vdots \\ v_M^1 & v_M^2 & \cdots & v_M^N \\ w_1^1 & w_1^2 & \cdots & w_1^N \\ w_2^1 & w_2^2 & \cdots & w_2^N \\ \vdots & \cdots & \cdots & \vdots \\ w_M^1 & w_M^2 & \cdots & w_M^N \end{bmatrix} \tag{9}$$

where N is the number of snapshot and M is the number of element componing the velocity vector. This lead us to calculate the autocovariance matrix as:

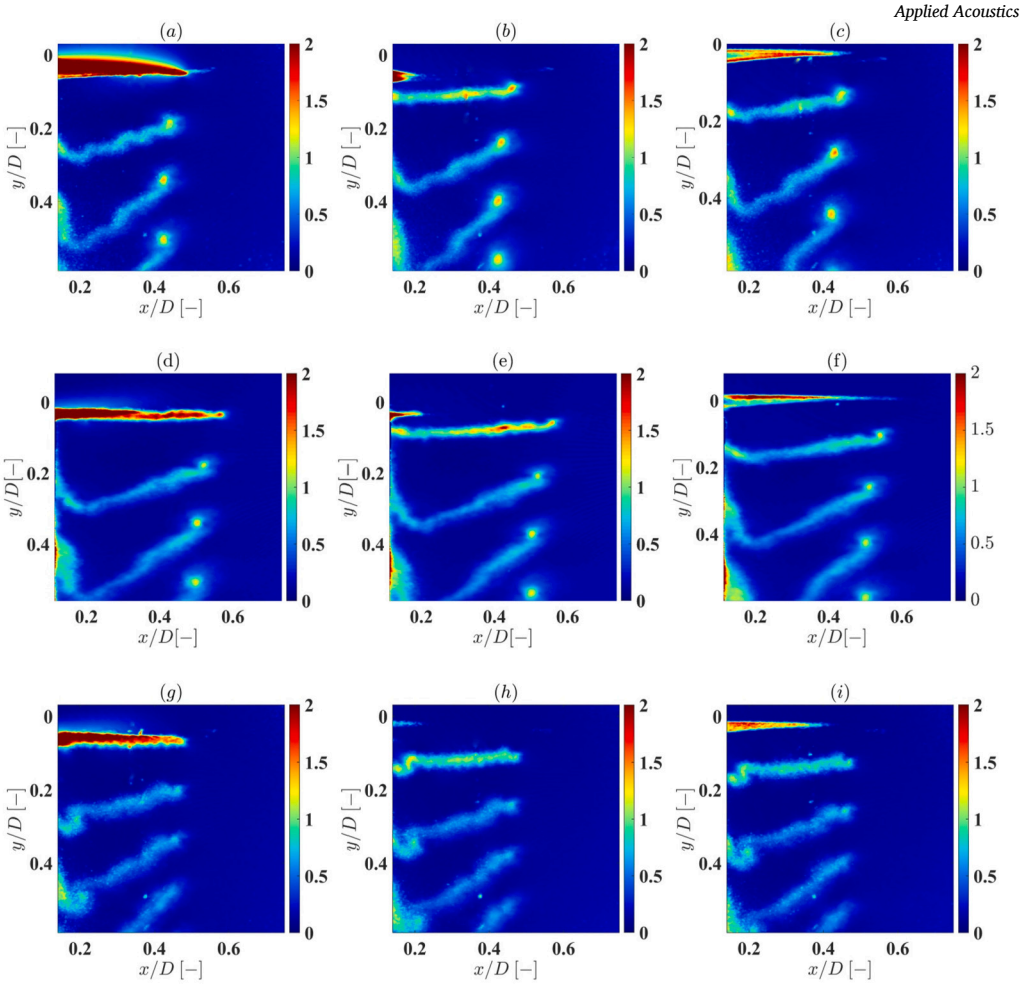

Fig. 14. Velocity rms distribution of the phase-locked PIV measurements for the baseline propeller (first row), the STE1 propeller (second row), and the STE2 propeller (third row) at inflow velocity $v_{fan} = 6\,\mathrm{m/s}$ and rotational speed $\Omega = 5000\,RPM$.

$$\tilde{\mathbf{C}} = \mathbf{U}^T\mathbf{U} \tag{10}$$

Then, the procedure is to resolve the corresponding eigenvalue problem:

$$\tilde{\mathbf{C}}\mathbf{A}^i = \lambda^i\mathbf{A}^i \tag{11}$$

and to re-order the obtained solutions by the size of the obtained eigenvalues:

$$\lambda^1 > \lambda^2 > .. > \lambda^N \tag{12}$$

The eigenvectors of the Eq. (11) compose the basis of the POD modes ϕ^i, defined as:

$$\phi^i = \frac{\sum_{n=1}^{N} A_n^i \mathbf{u}_n}{\| \sum_{n=1}^{N} A_n^i \mathbf{u}_n \|} \quad , \; i = 1, .., N \tag{13}$$

where A_n^i is the n-th component of the eigenvectors corresponding to λ^i of the Eq. (11) and the $\| \cdot \|$ represent the discrete 2-norm.
Each snapshot can be expanded in a series of the POD modes with expansion coefficients a_i, called POD coefficients, for each mode i. The POD coefficients are defined as the projection of the velocity fields fluctuating part onto the POD modes:

$$\mathbf{a}^N = \mathbf{\Psi}^T\mathbf{u}^N \tag{14}$$

the matrix $\mathbf{\Psi}$ is composed of the POD modes as $\mathbf{\Psi} = \left[\phi^1\, \phi^2 \ldots \phi^N\right]$. Therefore, the expansion of the fluctuating part of a single snapshot n is:

$$\mathbf{u}_n = \sum_{i=1}^{N} a_i^n \phi^i = \mathbf{\Psi}\mathbf{a}^n \tag{15}$$

The total kinetic energy of the velocity fluctuating component of a single snapshot is proportional to the eigenvalue λ_i [76], by having imposed the Eq. (12) it is ensured that the most energetic mode is the first one. Generally, this means that the first mode is associated with large-scale flow structures namely the dominant flow structures are reflected in the first POD mode. Therefore, the fluctuating velocity can be reconstructed correctly by using only the first few modes. To improve result clarity and highlight the most relevant structures, the POD analysis focused on a defined Region of Interest (*ROI*) that included only the inflow region.
Furthermore, to ensure the accuracy of the results, the convergence of the eigenvalues was assessed, and the results are presented in Fig. 15. This figure illustrates the trend of the first three normalized eigenvalues as a function of the number of snapshots N used to construct the matrix U for the baseline propeller, STE1, and STE2, shown in figures (a), (b), and (c), respectively. It can be observed that beyond $N = 150$, the value of each eigenvalue λ_i remains constant. This confirms that eigenvalue convergence has been achieved, indicating the reliability of the POD outcomes.
Before presenting the obtained results, the authors aim to introduce the main structures present in this type of problem and highlighted by this approach. Fig. 16 reports the first POD mode related to the baseline propeller as reference. The dominant structures include the hub vortex on the left side of the figure at $x/D = 0.15$, the tip vortex in the $x/D = 0.4$ region characterized by alternating positive and negative zones, and the trailing edge vorticity sheet, exhibiting a repeating horizontal pattern

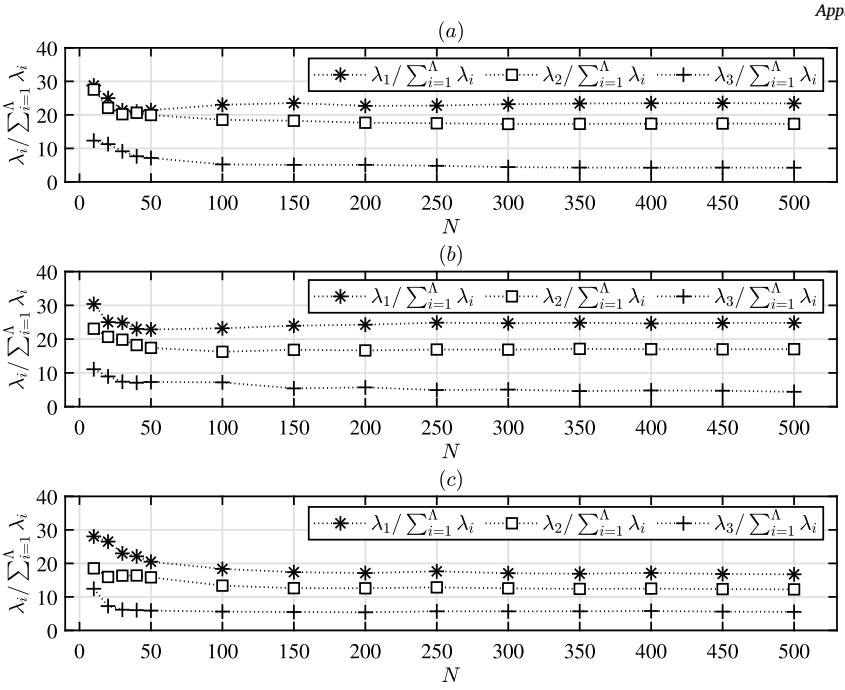

Fig. 15. Convergence analysis of POD eigenvalues as a function of the number of snapshots for the baseline (a), the STE1 (b), and the STE2 (c) propellers.

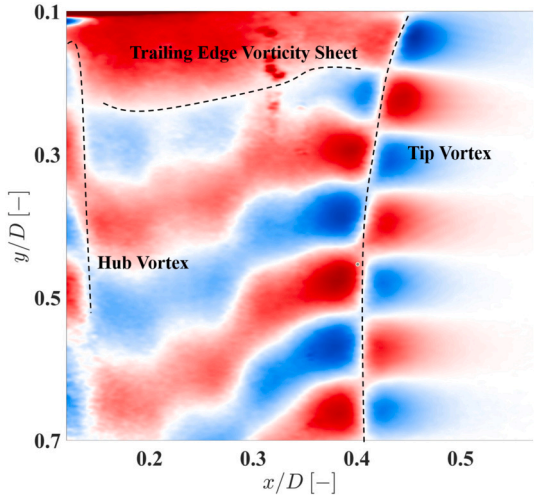

Fig. 16. Example of Proper Orthogonal Decomposition (POD) of a velocity field downstream of a propeller. The dashed lines highlight the main observable structures.

with a spatial frequency of approximately $0.1D$. These structures also represent the three primary noise sources, and evaluating the influence of serrations on them helps elucidate the noise reduction mechanism.

For conciseness, the reported results focus exclusively on the first and third modes for each propeller. These modes were chosen based on their higher energy levels. The second and fourth modes have been excluded as they are degenerate modes. Degenerate modes occur when one or more eigenvalues of the autocorrelation matrix are identical. The most common scenario involves two identical eigenvalues, known as "double modes," which are characteristic of a traveling wave [77], as in the present case. Consequently, the information obtained from the first and third modes is of general significance. The results obtained for the STE propellers compared to the BL are displayed in Fig. 17. The first row shows the trend of the first mode, while the second row presents the third mode for each propeller. The most evident result is a reversal of behavior between the baseline propeller and the STE propellers. For the baseline propeller, the three structures identified in Fig. 16 are observed, both for the first, Fig. 17(a), and third modes, Fig. 17(d). More in detail, the first mode exhibits a pattern of horizontal stripes repeating approximately every $0.1D$, while the same pattern is observed for the third mode, but with stripes repeating every $0.05D$, corresponding to half the wavelength. This indicates that between the first and third modes, a main dynamic (associated with the first mode) and an internal subdynamic (associated with the third mode) within the structure itself are identified. This is easily noticeable by also observing the tip vortices; in Fig. 17 (a), a bipolar trend is observed, while the third mode in the same area exhibits a quadrupole-like structure, that is the internal dynamics of the tip vortex. This behavior can be better appreciated in the enlargement reported in Fig. 18. What is very interesting is that the serrations tend to excite these dynamics, giving it enough energy to be projected onto the first mode (Fig. 17 (b)), since the third mode for the baseline moved to the first one for STE propellers. Furthermore, a general loss of coherence of the wake is observed for the STE1 propeller with the breakdown of trailing edge vorticity, which is no longer a continuous pattern but presents discontinuities. Such behavior can be interpreted as a loss of energy in trailing edge vorticity, which contributes to the reduction of broadband noise. An example of this effect is evident in the black squared region in Fig. 18. Another effect observed is that the serrations leave a trace at the trailing edge in the region x/D = 0.3-0.4, highlighted by the dashed line in Fig. 18. The third mode for the STE1 propeller (Fig. 17(e)) also confirms the breakdown of the spanwise correlation length. In fact, there is a blue streak up to $x/D = 0.25$, then becoming red. This is the most energetic structure associated with this mode, and it is seen how compared to the BL, its length has halved. This mechanism is the basis of the observed reduction in broadband noise in Figs. 7-10. Regarding the STE2 propeller, the first mode, like for the STE1, shows small-scale structures again, but compared to the other propeller, this time the presence of serrations along the entire trailing edge has further eliminated the spanwise correlation, greatly reducing the energy of the vorticity at the trailing edge, as can be seen in the circled region of Fig. 19(a), and the tip vortex, as reported in the enlargement of Fig. 19(a). Having a serration that covers a larger surface, this dynamic has completely lost coherence and is no longer easily distinguishable. This is also seen in the third mode in the region $y/D = 0.1$, which previously consisted of a clear streak but now has an alternating positive-negative trend. Such effect is enlarged in Fig. 19(b) where a

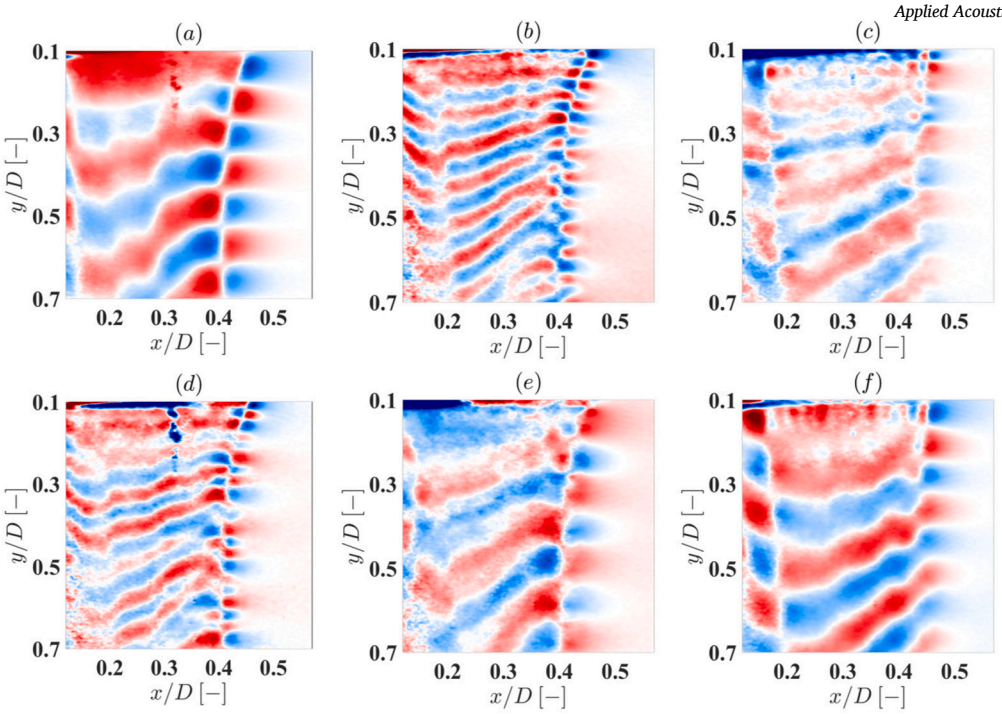

Fig. 17. POD modes for the u-component of velocity vector in advanced flight condition at $v = 6$ m/s and $\Omega = 5000\,RPM$: (a) first POD mode for the baseline propeller; (b) first POD mode for the STE1 propeller; (c) first POD mode for the STE2 propeller; (d) third POD mode for the baseline propeller; (e) third POD mode for the STE1 propeller; (f) third POD mode for the STE2 propeller.

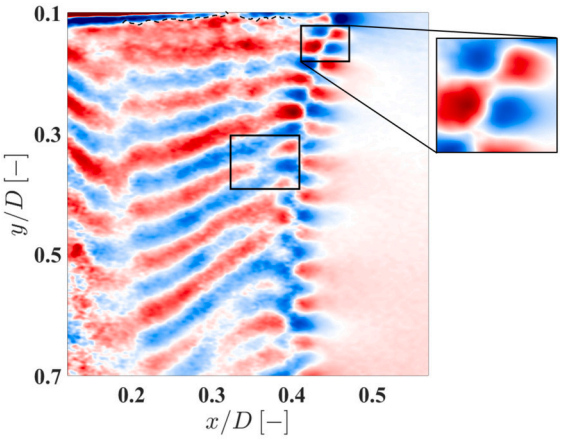

Fig. 18. First POD mode for the STE1 propeller with an enlargement of the tip vortex.

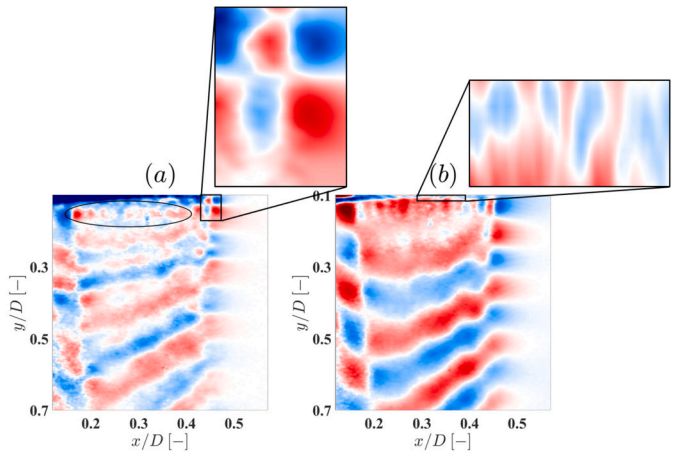

Fig. 19. First (a) and third(b) POD modes for the STE2 propeller with an enlargement of the tip vortex and the trailing edge vorticity region.

bubble-like behavior can be observed. The results are consistent with Prigent et al. [32] and Wei et al. [78] which demonstrate that TE serration induces a significant reduction of spanwise correlation and wake coherence. As demonstrated by Gu et al. [3], the presence of serrations modifies the vortex structure, leading to a reduction in vortex intensity. In particular, a decrease in the shear layer length of the tip vortices and a reduction in the central vortex scale are observed compared to the BL configuration. These changes result in lower velocity and pressure at the propeller tip, thereby reducing noise fluctuations and supporting the overall decrease in aerodynamic noise.

The analysis of Proper Orthogonal Decomposition (POD) modes reveals that both STE propellers exhibit a correlation length approximately equal to half the blade span. Consequently, it can be concluded that covering only half of the span is sufficient to achieve acoustic effectiveness. Increasing the number of serrations and extending their coverage further along the trailing edge does not provide additional benefits. Specifically, serrations located near the hub appear to be inactive, likely due to pre-existing flow separation in that region.

4. Conclusions

A total of 23 propellers were manufactured with a sawtooth pattern applied at the trailing edge, and their noise signature was investigated. The initial phase consists of an experimental analysis of the tooth impact on noise emissions in hovering conditions. The OASPL was employed as a metric to evaluate the noise performance revealing a possible noise reduction of 3-4 dB. It was observed that careful attention is required during the design of STE propellers, as an improper serration design can potentially lead to an increase in propeller noise. From these results, two configurations were selected for further testing. The investigation of directivity, both for the Overall and the Band Limited SPL, together with spectral analysis, shows how the use of serrations influences both tonal

and broadband noise.

The expected reduction in broadband noise aligns with previous studies in the literature. However, the effect on tonal noise has not been observed yet. Furthermore, the results highlight a strong directivity, suggesting the presence of preferential regions where the use of serrations is more advantageous. In addition, the statistical analysis, in terms of Probability Density Functions, indicates a damping in the tails of the distribution function for the STE propellers compared to the baseline. Such results motivate a deeper investigation to enhance our understanding of the problem.

This second part aimed at examining the aerodynamic and aeroacoustic properties of STE propellers, as well as analyzing the velocity field downstream of the propeller, in hovering and forward flight conditions. The analysis of the thrust coefficient shows a reduction in the thrust force, consistent with existing literature, amounting to approximately 10-15%. This result suggests the implementation of this control strategy should be carefully considered and limited to specific applications where the loss in thrust does not compromise mission success.

Furthermore, the far-field microphone measurements reveal a noise reduction of almost 3-4 dB over the entire polar angle range in the presence of an inflow velocity. However, in hovering conditions, the noise emissions are concentrated in a specific polar angle range. The statistical analysis once again highlights a departure from Gaussian distribution in advanced flight conditions, indicating the presence of coherent structures within the time history, damped by serrations. The mitigation of coherent structures could be the first hypothesis to interpret the mechanism underlying broadband noise reduction.

For this purpose, the flow field around the blade has been characterized using PIV. The mean velocity and root main square velocity fields indicate a reduction in the wake velocity and the tip vortex intensity. Moreover, the root main square velocity field obtained by phase-locked PIV measurements shows also a lower intensity and faster dissipation of the trailing edge vorticity sheet along the entire blade, which represents the primary cause of broadband noise reduction. A Proper Orthogonal Decomposition analysis has been performed on the velocity field to gain further insights. The main outcome is a reduction in the wake coherency and a modification of the spanwise fluid-dynamic correlation length, which may be intended as the origin of the broadband noise mitigation. Furthermore, the serrations excite small-scale structures associated with the dynamics of the tip vortex and trailing edge vorticity, which become dominant. The larger-scale structures have thus lost energy, and this mechanism may account for the observed noise reduction.

In conclusion, the use of serration at the trailing edge as a passive control strategy to reduce the noise emission of a small drone proves to be highly promising. This approach is particularly attractive for applications that demand minimal noise impact, such as urban environments, or that prioritize reduced motion range, such as infrastructure reconnaissance or mining operations. In these scenarios, a trade-off between thrust reduction and noise reduction can be accepted, making serrations a viable solution.

CRediT authorship contribution statement

Paolo Candeloro: Writing – review & editing, Writing – original draft, Methodology, Investigation, Formal analysis, Data curation, Conceptualization. **Daniele Ragni:** Writing – review & editing, Methodology, Investigation. **Tiziano Pagliaroli:** Writing – review & editing, Methodology, Formal analysis, Conceptualization.

Declaration of generative AI and AI-assisted technologies in the writing process

During the preparation of this work the author(s) used ChatGPT in order to o improve the readability and language of the manuscript. After using this tool/service, the author(s) reviewed and edited the content as needed and take(s) full responsibility for the content of the published article.

Declaration of competing interest

The authors declare that they have no known competing financial interests or personal relationships that could have appeared to influence the work reported in this paper.

Acknowledgements

The authors would like to express sincere gratitude to Edoardo Grande for his invaluable assistance during the testing phase and for providing access to the facilities at Delft University of Technology. Special thanks also to Ranieri Nargi for his support throughout the testing process. This work has been made possible thanks to the collaborative efforts between Università Niccolò Cusano and Delft University of Technology.

Data availability

Data will be made available on request.

References

[1] Floreano D, Wood RJ. Science, technology and the future of small autonomous drones. Nature 2015;521:460–6. https://doi.org/10.1038/nature14542.

[2] Bu H, Wu H, Bertin C, Fang Y, Zhong S. Aerodynamic and acoustic measurements of dual small-scale propellers. J Sound Vib 2021;511:116330. https://doi.org/10.1016/j.jsv.2021.116330.

[3] Gu Y, Song F, Bai H, Wu J, Liu K, Nie B, et al. Numerical and experimental studies on the owl-inspired propellers with various serrated trailing edges. Appl Acoust 2024;220:109948. https://doi.org/10.1016/j.apacoust.2024.109948.

[4] Höhrová P, Soviar J, Sroka W. Market analysis of drones for civil use. LOGI Sci J Transp Logist 2023;14:55–65.

[5] Gur O, Rosen A. Optimizing electric propulsion systems for unmanned aerial vehicles. J Aircr 2009;46:1340–53. https://doi.org/10.2514/1.41027.

[6] Gur O, Rosen A. Design of a quiet propeller for an electric mini. J Propuls Power 2009;25:717–28. https://doi.org/10.2514/1.38814.

[7] Pagliaroli T, Candeloro P, Camussi R, Giannini O, Panciroli R, Bella G. Aeroacoustic study of small scale rotors for mini drone propulsion: serrated trailing edge effect. In: 2018 AIAA/CEAS aeroacoustics conference; 2018.

[8] Sinibaldi G, Marino L. Experimental analysis on the noise of propellers for small UAV. Appl Acoust 2013. https://doi.org/10.1016/j.apacoust.2012.06.011.

[9] Pagliaroli T, Moschetta J, Benard E, Nana C. Noise signature of a mav rotor in hover. In: 49th international symposium of applied aerodynamics; 2014. p. 24–5.

[10] JanakiRam D, Scruggs B. Investigation of performance, noise and detectability characteristics of small-scale remotely piloted vehicle /RPV/ propellers. In: 7th aeroacoustics conference, vol. 19; 1981. p. 1052–60.

[11] Serré R, Chapin V, Moschetta J-M, Fournier H. Reducing the noise of micro-air vehicles in hover. In: International micro air vehicle conference and flight competition; 2017. p. 51–9. Available from: https://hal.science/hal-02407208.

[12] Leslie A, Wong K, Auld D. Broadband noise reduction on a mini-UAV propeller. In: 14th AIAA/CEAS aeroacoustics conference (29th AIAA aeroacoustics conference); 2008. p. 3069.

[13] Nelson P, Morfey C. Aerodynamic sound production. J Sound Vib 1981;79:263–89. https://doi.org/10.1016/0022-460X(81)90372-2.

[14] Rozenberg Y, Roger M, Moreau S. Rotating blade trailing-edge noise: experimental validation of analytical model. AIAA J 2010. https://doi.org/10.2514/1.43840.

[15] Candeloro P, Martellini E, Nederlof R, Sinnige T, Pagliaroli T. An experimental study of the aeroacoustic properties of a propeller in energy harvesting configuration. Fluids 2022;7. https://doi.org/10.3390/fluids7070217. Available from: https://www.mdpi.com/2311-5521/7/7/217.

[16] Leslie A, Wong K, Auld D. Experimental analysis of the radiated noise from a small propeller. In: Proceedings of 20th international congress on acoustics, ICA. Madrid, Spain: International Commission for Acoustics; 2010. p. 23–7.

[17] Pang E, Cambray A, Rezgui D, Azarpeyvand M, Showkat-Ali S. Investigation towards a better understanding of noise generation from UAV propellers. In: 2018 AIAA/CEAS aeroacoustics conference; 2018. p. 3450.

[18] Candeloro P, Ragni D, Pagliaroli T. Small-scale rotor aeroacoustics for drone propulsion: a review of noise sources and control strategies. Fluids 2022;7:279. https://doi.org/10.3390/fluids7080279.

[19] Del Duchetto F, Pagliaroli T, Candeloro P, Rossignol K, Yin J. Aeroacoustic study of synchronized rotors. Aerospace 2025;12:162. https://doi.org/10.3390/aerospace12020162.

[20] Howe M. Noise produced by a sawtooth trailing edge. J Acoust Soc Am 1991;90:482–7. https://doi.org/10.1121/1.401273.
[21] Howe M. Aerodynamic noise of a serrated trailing edge. J Fluids Struct 1991;5:33–45. https://doi.org/10.1016/0889-9746(91)80010-B.
[22] Lyu B, Azarpeyvand M, Sinayoko S. Prediction of noise from serrated trailing edges. J Fluid Mech 2016;793:556–88. https://doi.org/10.1017/jfm.2016.132.
[23] Huang X. Theoretical model of acoustic scattering from a flat plate with serrations. J Fluid Mech 2017;819:228–57. https://doi.org/10.1017/jfm.2017.176.
[24] Ragni D, Avallone F, van der Velden WC. Concave serrations on broadband trailing edge noise reduction. In: 23rd AIAA/CEAS aeroacoustics conference; 2017. p. 4174.
[25] Avallone F, Van Der Velden W, Ragni D, Casalino D. Noise reduction mechanisms of sawtooth and combed-sawtooth trailing-edge serrations. J Fluid Mech 2018. https://doi.org/10.1017/jfm.2018.377.
[26] van der Velden WC, van Zuijlen A, Ragni D. Flow topology and noise emission around straight, serrated and slitted trailing edges using the lattice Boltzmann methodology. In: 22nd AIAA/CEAS aeroacoustics conference; 2016. p. 3021.
[27] León C, Merino-Martínez R, Ragni D, Avallone F, Scarano F, Pröbsting S, et al. Effect of trailing edge serration-flow misalignment on airfoil noise emissions. J Sound Vib 2017;405:19–33. https://doi.org/10.1016/j.jsv.2017.05.035.
[28] Arce Leon C, Avallone F, Pröbsting S, Ragni D. Piv investigation of the flow past solid and slitted sawtooth serrated trailing edges. In: 54th AIAA aerospace sciences meeting; 2016. p. 1014.
[29] Nedić J, Vassilicos JC. Vortex shedding and aerodynamic performance of airfoil with multiscale trailing-edge modifications. AIAA J 2015;53:3240–50. https://doi.org/10.2514/6.2016-1014.
[30] Ning Z, Hu H. An experimental study on the aerodynamics and aeroacoustic characteristics of small propellers. In: 54th AIAA aerospace sciences meeting; 2016. p. 1785.
[31] Chong T, Vathylakis A. On the aeroacoustic and flow structures developed on a flat plate with a serrated sawtooth trailing edge. J Sound Vib 2015. https://doi.org/10.1016/j.jsv.2015.05.019.
[32] Prigent S, Buxton O, Bruce P. Wake of a lifting wing with cut-in sinusoidal trailing edges. AIAA J 2017;55:1590–601. https://doi.org/10.2514/1.J055068.
[33] Ning Z, Hu H. An experimental study on the aerodynamic and aeroacoustic performances of a bio-inspired UAV propeller. In: 35th AIAA applied aerodynamics conference; 2017. p. 3747.
[34] Intravartolo N, Sorrells T, Ashkharian N, Kim R. Attenuation of vortex noise generated by UAV propellers at low Reynolds numbers. In: 55th AIAA aerospace sciences meeting; 2017. p. 2019.
[35] Candeloro P, Ragni D, Pagliaroli T. Unconventional application of serrated trailing edges for quieter propeller drones. In: 30th AIAA/CEAS aeroacoustics conference; 2024. p. 3107.
[36] Li Y, Yang Y, Liu Y, Wang Y, Huang B, Li W. Aerodynamic and aeroacoustic analyses of a uav propeller with trailing edge serrations. In: Proceedings of ACOUSTICS, vol. 7. 2018.
[37] Oerlemans S, Fisher M, Maeder T, Kögler K. Reduction of wind turbine noise using optimized. AIAA J 2009;47. https://doi.org/10.2514/1.38888.
[38] Lee HM, Lu Z, Lim KM, Xie J, Lee HP. Quieter propeller with serrated trailing edge. Appl Acoust 2019;146:227–36. https://doi.org/10.1016/j.apacoust.2018.11.020.
[39] Yang Y, Wang Y, Liu Y, Hu H, Li Z. Noise reduction and aerodynamics of isolated multi-copter rotors with serrated trailing edges during forward flight. J Sound Vib 2020;489:115688. https://doi.org/10.1016/j.jsv.2020.115688.
[40] Yang Y, Liu Y, Hu H, Liu X, Wang Y, Arcondoulis EJ, et al. Experimental study on noise reduction of a wavy multi-copter rotor. Appl Acoust 2020;165:107311. https://doi.org/10.1016/j.apacoust.2020.107311.
[41] Gruber M, Azarpeyvand M, Joseph P. Airfoil trailing edge noise reduction by the introduction of sawtooth and slitted trailing edge geometries. In: Proceedings of 20th international congress on acoustics, vol. 10. 2010. p. 6.
[42] Moreau D, Doolan CJ. Noise-reduction mechanism of a flat-plate serrated trailing edge. AIAA J 2013;51:2513–22. https://doi.org/10.2514/1.J052436.
[43] Moreau D, Brooks L, Doolan C. On the noise reduction mechanism of a flat plate serrated trailing edge at low-to-moderate Reynolds number. In: 18th AIAA/CEAS aeroacoustics conference (33rd AIAA aeroacoustics conference); 2012. p. 2186.
[44] Mancinelli M, Jordan P, Lebedev A, Kari R. Real-time jet-plate interaction noise estimation based on near-field sensor readings. In: 28th AIAA/CEAS aeroacoustics 2022 conference; 2022. p. 2871.
[45] Mancinelli M, Jordan P, Lebedev A, Kari R. Exploring flexible trailing edge properties to reduce installed jet noise in a jet-plate configuration. In: 28th AIAA/CEAS aeroacoustics 2022 conference; 2022. p. 2872.
[46] Amiet R. Noise due to turbulent flow past a trailing edge. J Sound Vib 1976;47:387–93. https://doi.org/10.1016/0022-460X(76)90948-2.
[47] Blandeau V, Joseph P. Validity of Amiet's model for propeller trailing-edge noise. AIAA J 2011;49:1057–66. https://doi.org/10.2514/1.J050765.
[48] Pierce A. Acoustics: an introduction to its physical principles and applications. Springer; 2019.
[49] Di Marco A, Mancinelli M, Camussi R. Pressure and velocity measurements of an incompressible moderate Reynolds number jet interacting with a tangential flat plate. J Fluid Mech 2015;770:247–72. https://doi.org/10.1017/jfm.2015.149.
[50] Mancinelli M, Pagliaroli T, Di Marco A, Camussi R, Castelain T. Wavelet decomposition of hydrodynamic and acoustic pressures in the near field of the jet. J Fluid Mech 2017;813:716–49. https://doi.org/10.1017/jfm.2016.869.
[51] Leishman G. Principles of helicopter aerodynamics with CD extra. Cambridge University Press; 2006.
[52] McCormick B. Aerodynamics, aeronautics, and flight mechanics. John Wiley; 1995.
[53] Manolesos M, Voutsinas SG. Experimental study of drag-reduction devices on a flatback airfoil. AIAA J 2016;54:3382–96. https://doi.org/10.2514/1.J054901.
[54] Wang J, Zhang C, Wu Z, Wharton J, Ren L. Numerical study on reduction of aerodynamic noise around an airfoil with biomimetic structures. J Sound Vib 2017;394:46–58. https://doi.org/10.1016/j.jsv.2016.11.021.
[55] Treuren KV, Wisniewski C. Testing propeller tip modifications to reduce acoustic noise generation on a quadcopter propeller. J Eng Gas Turbines Power 2019;141:121017. https://doi.org/10.1115/1.4044971.
[56] Farge M. Wavelet transforms and their applications to turbulence. Annu Rev Fluid Mech 1992;24:395–458. https://doi.org/10.1146/annurev.fl.24.010192.002143.
[57] Farge M, Schneider K. Wavelet transforms and their applications to mhd and plasma turbulence: a review. J Plasma Phys 2015;81:435810602. https://doi.org/10.1017/S0022377815001075.
[58] Lau K, Weng H. Climate signal detection using wavelet transform: how to make a time series sing. Bull Am Math Soc 1995;76:2391–402. https://doi.org/10.1175/1520-0477(1995)076<2391:CSDUWT>2.0.CO;2.
[59] Camussi R, Guj G. Orthonormal wavelet decomposition of turbulent flows: intermittency and coherent structures. J Fluid Mech 1997;348:177–99. https://doi.org/10.1017/S0022112097006551.
[60] Mallat S. A theory for multiresolution signal decomposition: the wavelet representation. IEEE Trans Pattern Anal Mach Intell 1989;11:674–93. https://doi.org/10.1109/34.192463.
[61] Daubechies I. Ten lectures on wavelets. SIAM; 1992.
[62] Torrence C, Compo G. A practical guide to wavelet analysis. Bull Am Meteorol Soc 1998;79:61–78. https://doi.org/10.1175/1520-0477(1998)079<0061:APGTWA>2.0.CO;2.
[63] Pagliaroli T, Camussi R. Wall pressure fluctuations in rectangular partial enclosures. J Sound Vib 2015;341:116–37. https://doi.org/10.1016/j.jsv.2014.12.008.
[64] Pagliaroli T, Mancinelli M, Troiani G, Iemma U, Camussi R. Fourier and wavelet analyses of intermittent and resonant pressure components in a slot burner. J Sound Vib 2018;413:205–24. https://doi.org/10.1016/j.jsv.2017.10.029.
[65] Pagliaroli T, Troiani G. Wavelet and recurrence analysis for lean blowout detection: an application to a trapped vortex combustor in thermoacoustic instability. Phys Rev Fluids 2020;5:073201. https://doi.org/10.1103/PhysRevFluids.5.073201.
[66] Kim DH, Park C, Moon Y. Aerodynamic analyses on the steady and unsteady loading-noise sources of drone propellers. Int J Aeronaut Space Sci 2019;20:611–9. https://doi.org/10.1007/s42405-019-00176-3.
[67] Miljković D, Ivošević J, Bucak T. Two vs. three blade propeller-cockpit noise comparison. In: 5th congress of Alps-Adria acoustics association; 2012.
[68] Lumley JL. The structure of inhomogeneous turbulent flows. In: Atmospheric turbulence and radio wave propagation; 1967. p. 166–78.
[69] Meyer K, Pedersen J, Özcan O. A turbulent jet in crossflow analysed with proper orthogonal decomposition. J Fluid Mech 2007;583:199–227. https://doi.org/10.1017/S0022112007006143.
[70] Magionesi F, Dubbioso G, Muscari R, Di Mascio A. Modal analysis of the wake past a marine propeller. J Fluid Mech 2018;855:469–502. https://doi.org/10.1017/jfm.2018.631.
[71] Sirovich L. Turbulence and the dynamics of coherent structures. III. Dynamics and scaling. Q Appl Math 1987;45:583–90. https://doi.org/10.1090/qam/910464.
[72] Berkooz G, Holmes P, Lumley J. The proper orthogonal decomposition in the analysis of turbulent flows. Annu Rev Fluid Mech 1993;25:539–75. https://doi.org/10.1146/annurev.fl.25.010193.002543.
[73] Andrianne T, Razak N, Dimitriadis G, Okamoto S. Flow visualization and proper orthogonal decomposition of aeroelastic phenomena. In: Wind tunnels; 2011. p. 87–104.
[74] Aubry N. On the hidden beauty of the proper orthogonal decomposition. Theor Comput Fluid Dyn 1991;2:339–52. https://doi.org/10.1007/BF00271473.
[75] Kerschen G, Golinval J, Vakakis A, Bergman L. The method of proper orthogonal decomposition for dynamical characterization and order reduction of mechanical systems: an overview. Nonlinear Dyn 2005;41:147–69. https://doi.org/10.1007/s11071-005-2803-2.
[76] Fukunaga K. Introduction to statistical pattern recognition. 2nd ed. USA: Academic Press Professional, Inc.; 1990.
[77] Hasan N, Sanghi S. Proper orthogonal decomposition and low-dimensional modelling of thermally driven two-dimensional flow in a horizontal rotating cylinder. J Fluid Mech 2007;573:265–95. https://doi.org/10.1017/S0022112006003806.
[78] Wei Z, Wang S, Farris S, Chennuri N, Wang N, Shinsato S, et al. Towards silent and efficient flight by combining bioinspired owl feather serrations with cicada wing geometry. Nature 2024;15:4337. https://doi.org/10.1038/s41467-024-48454-3.